Volume 1 | Number 1 | Jan 2013 | Pages 1–100

## Nanoscale

www.rsc.org/nanoscale

# Journal Name

## ARTICLE

# Lorentz microscopy sheds light on the role of dipolar interactions in magnetic hyperthermia

M. Campanini[a]*, R. Ciprian[a], E. Bedogni[b], A. Mega[b], V. Chiesi[a], F. Casoli[a], C. de Julián Fernández[a], E. Rotunno[a], F. Rossi[a], A. Secchi[b], F. Bigi[b], G. Salviati[a], C. Magén[c], V. Grillo[a] and F. Albertini[a]

Monodispersed $Fe_3O_4$ nanoparticles with comparable size distributions have been synthetized by two different synthesis routes, co-precipitation and thermal decomposition. Thanks to the different steric stabilization, the described samples can be considered as a model system to investigate the effects of magnetic dipolar interactions on the aggregation states of the nanoparticles. Moreover, the presence of magnetic dipolar interactions can strongly affect the nanoparticles efficiency as hyperthermic mediator. In this paper we present a novel way to visualize and map the magnetic dipolar interactions in different kind of nanoparticle aggregates by the use of Lorentz microscopy, an easy and reliable in-line electron holographic technique. Exploiting Lorentz microscopy, which is complementary to the magnetic measurements, it is possible to correlate the interaction degrees of magnetic nanoparticles to their magnetic behaviors. In particular, we demonstrate that Lorentz microscopy is successful in visualizing the magnetic configurations stabilized by dipolar interactions, thus paving the way to the comprehension of the power losses mechanisms for different nanoparticle aggregates.

## 1. Introduction

In the last decade, many efforts have been devoted to the research of new nanostructured materials with functional properties that can be exploited in biomedical applications.[1] Magnetic nanoparticles (NPs) in the superparamagnetic state are suitable for both diagnostic and therapeutic approaches. In the field of diagnostics, they have been proposed as a contrast agent to enhance the magnetic resonance imaging (MRI) signal,[2-5] while in the field of therapeutics they can be used as magnetic vectors in drug delivery[6-9] and/or heat mediators in hyperthermia treatment.[10, 11]

Magnetic NPs are a unique tool for their reduced size that allows a direct intravenous injection, their delivery through the blood vessels and the possibility of functionalization with specific targeting molecules due to the high surface to volume ratio. Thanks to their magnetic properties, they can be detected, driven toward a specific target by exploiting magnetic field gradients and heated by radiofrequency magnetic fields. This last property is at the basis of magnetic hyperthermia.

Magnetic hyperthermia can be effectively employed to locally induce cancer cell death. The ability of a material to be a good hyperthermic mediator is measured by the specific power absorption (SPA), which represents the thermic power developed by the magnetic NPs per unit mass under an applied external alternating (AC) magnetic field. The transformation of the AC field energy into heat occurs by several mechanisms and the process efficiency strongly depends on the frequency and amplitude of the external field, as well as on particle size, shape and inter-particle interactions.[12] The hyperthermia efficiency can be therefore improved by adjusting and tuning these parameters, permitting the use of (i) lower magnetic NPs amounts and (ii) fields at lower frequency and amplitudes. Presently, the scientific community is working on three different fronts for achieving this aim: the material, the optimization of NP size, and the development of an optimal shape.

Among the biocompatible materials, magnetite has been demonstrated to be very promising, mainly because it can be obtained in big amounts and by easy synthesis routes in a nanostructured form, with a good control of both size and shape.[13,14] On the magnetic side, the choice of the material is driven by the requirements on the magneto-crystalline anisotropy, an intrinsic property depending on composition and crystal structure, which influences the hysteresis loop shape and the critical size for the transition from the superparamagnetic to the ferromagnetic regime (higher is the anisotropy value, smaller is the critical size). This intrinsic property strongly influences the SPA value, which has been demonstrated to be maximum in proximity of this critical size.[15] At the same time, also the variation of the NP shape can produce an increase of the magnetic anisotropy by adding two non-negligible terms:

shape anisotropy, directly related to the shape of magnetic NPs, and surface anisotropy, which is influenced by the faceting of the magnetic NPs.[16, 17]

The SPA of magnetite NPs under an external alternating magnetic field is mainly due to two kinds of power loss mechanisms, hysteresis and relaxation loss,[18] while the contribution from eddy currents is negligible, due to the low conductivity of magnetite. Both these mechanisms are strongly influenced by the size of nanoparticles and the aggregation state.[14] In an ideal system of isolated superparamagnetic NPs, the absence of coercivity and remanence prevents the establishing of magnetic inter-particle interactions and the agglomeration, that could strongly affect the in-cell viability of the nanoparticles.[19,20] In real systems, however, inter-particle interactions can occur; dipolar interactions among particles strongly influence the heating power of the colloidal suspensions, but their role is not completely understood. Urtiberea et al.,[21] Presa et al.,[22] Serantes et al.[23] and Sadat et al.[24] found that SPA decreases with increasing the nanoparticles aggregation, whereas Martinez-Boubeta et al.,[25] Burrows et al.[26] and Jeun et al.[27] have demonstrated the beneficial effect of dipolar interactions on SPA. The recently proposed model of Landi et al.[28] shows that SPA could increase or decrease depending on the σ value (representing the ratio between the height of the energy barrier and the thermal energy); in particular, for small nanoparticles in the low-barrier regime, characterized by frequent jumps of the magnetization between the two energy minima but with a small energy release in each jump, dipolar interactions should increase the SPA value. Nonetheless, an in-depth analysis able to correlate the morphology of NPs aggregates forming due to interactions with the hyperthermic behavior is still lacking.

In this work, we present a novel way to visualize and map the inter-particle interactions employing Lorentz microscopy, a reliable technique that can be exploited even in transmission electron microscopes not equipped with an electron biprism. The reported characterization is performed on a model system, consisting of magnetite NPs with different degrees of interaction. In order to study a strongly interacting system, we have synthetized magnetite nanoparticles by the co-precipitation method without adding any stabilizing surfactant.

In comparison, a weakly interacting system has been obtained by the thermal decomposition synthesis, in which the presence of surfactant leads to a stably dispersed system. Recent works on Lorentz microscopy and electron holography reported ferromagnetic domains stabilized by dipolar interactions between NPs that are blocked at room temperature, while our model system consists of superparamagnetic magnetite NPs.[29-31] Furthermore, to the best of our knowledge, Lorentz microscopy has never been exploited to investigate the effects of magnetic interactions on the performance of NP suspensions as hyperthermic mediators; herein, we show how Lorentz microscopy can be advantageous to correlate the hyperthermic behavior of NPs to their aggregation state at the sub-micrometric scale.

## 2. Materials and methods

### 2.1. Synthesis of $Fe_3O_4$ nanoparticles

The synthesis by co-precipitation route was carried out following the procedure reported in Ref. 32 and schematically depicted in Fig. 1a. In particular, 4 g of $FeCl_2·4H_2O$ (20 mmol) were added to a solution of 11 g of $FeCl_3 ·6H_2O$ (40 mmol) in 120 mL of deionized water. The solution was heated at 360 K under Ar atmosphere. The pH value of the solution was adjusted to 10 by the addition of concentrated aqueous ammonia. The magnetite formation started immediately. After stirring for 4 h under argon atmosphere the reaction was cooled to room temperature (RT). The nanoparticles were washed several times with deionized water to remove the excess of ammonia. The black precipitate was collected by magnetic decantation, dried under high vacuum and characterized. The product was easily redispersed in aqueous solution by sonication for 5 mins. In the following, this sample will be referred to as CO-NPs. The synthesis by thermal decomposition was performed employing a slightly modified version of the procedure reported in Ref. 33 and summarized in Fig. 1b. $Fe(acac)_3$ (2 mmol), 1,2-hexadecanediol (10 mmol), oleic acid (6 mmol) and oleylamine (6 mmol) were mixed in 20 mL of benzyl ether under $N_2$ flow. The mixture was heated at 473 K for 2 h and then heated to reflux (~573 K) for 1 h under a $N_2$ blanket. When the black-brown mixture reached RT, ethanol (40 mL) was added. A black material was precipitated and separated by centrifugation (5000 rpm, 15 mins). The product was easily redispersed in hexane. In the following, this sample will be referred to as TD-NPs.

### 2.2. Structural, morphological and magnetic characterizations

The NPs specimens for transmission electron microscopy (TEM) analysis were prepared by depositing a drop of the diluted colloidal suspensions (1 mg / 10 mL) above the TEM grids. NPs size and morphology were investigated by TEM using a JEOL JEM-2200FS, operating at 200 kV; in particular, high-resolution electron microscopy (HREM) and electron diffraction (ED) were employed in nanoparticles characterization. The histograms corresponding to particle
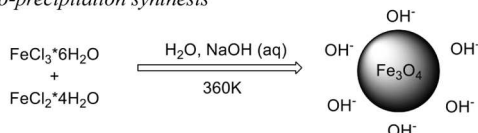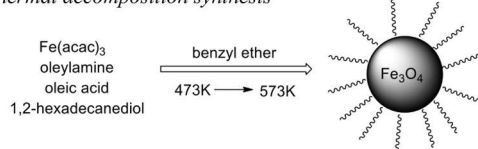


**Fig. 1** Schematic representation of the two synthesis routes: (a) co-precipitation, (b) thermal decomposition.

diameter distribution were fitted with a lognormal function (Fig 2c, f). The histograms were constructed by measuring the diameter of the NPs of several regions, including agglomerates. The value of <D> reported in the following is the mean particle diameter and $\sigma$ is the standard deviation of the distribution.[34,35] Lorentz microscopy was performed at room temperature turning off the objective lens and using the objective mini-lens as a Lorentz lens. In this way, the specimens are inserted in the TEM column in a field-free environment. Applying the Transport of Intensity Equation (TIE) to a Fresnel focal series (each frame of the series was acquired with an exposure of 1 sec), the phase can be retrieved.[36] The reconstruction can be directly computed within STEMCELL software[37], exploiting the recently introduced tool for Lorentz microscopy.[38] Moreover, taking a second focal series after turning upside-down the sample, it is possible to separate the electrostatic and magnetic contributions to the phase shift; afterwards, a map of the in-plane projected magnetic induction can be directly obtained differentiating the magnetic phase shift.[39] For the employed instrumental configuration, a resolution of about 10 nm is achievable in Lorentz microscopy mode.

The aggregation state of the nanoparticles in the colloidal suspension was studied employing Dynamic Light Scattering (DLS), using 90 Plus instrument (Brookhaven Instruments Corp.) equipped with 632 nm laser. The hydrodynamic diameter $D_h$ measured by DLS is a parameter influenced by many factors, such as particles coating and aggregation.[40]

The magnetization loops at RT of the NP samples were obtained either by Alternating Gradient Force Magnetometer (AGFM) or by Vibrating Sample Magnetometer (VSM); in both cases the maximum applied field was 2 T. In order to have a complete magnetic characterization, the Zero Field Cooling (ZFC) and Field Cooling (FC) measurements were obtained on dry samples by a Superconducting Quantum Interference Device (SQUID) magnetometer. The powders, dried into a capsule, are cooled down to 5 K; then, an external magnetic field of 7.96 kA/m is applied and the magnetic moment is measured during the heating up to RT (ZFC). The sample is then cooled again in the same external magnetic field and the moment is measured during the further heating (FC). From these two subsequent measurements the blocking temperature $(T_B)$ is obtained as the temperature at which the ZFC shows a maximum; the irreversibility temperature $(T_I)$ is estimated as the temperature at which the ZFC-FC curves start to be separated and the saturation temperature $(T_S)$ is defined as the temperature at which the FC stops to be constant. For a non-ideal system of poly-dispersed NPs, $T_B$ can be considered as the average blocking temperature. Under $T_B$ nanoparticles are blocked while, over $T_B$ they are in the superparamagnetic state. The $T_I$, instead, can be considered as the maximum blocking temperature corresponding to the blocking temperature of the biggest magnetic NPs. The $T_S$, on the contrary, is the minimum blocking temperature of the array for the smallest nanoparticles.

Hyperthermia measurements were obtained on colloidal suspensions of nanoparticles with a concentration smaller than 1% wt. dispersed in organic solvents (hexane) or water, by

means of an AC commercial applicator (nanoScale Biomagnetics DM100), applying a field with 12.7 kA/m amplitude and 235 kHz frequency. The temperature increase was measured through an optical fiber thermometer to avoid the coupling with the radiofrequency field. Temperature sensitivity was 0.1 K. The SPA value, measured in W/g, can be defined as:

$$SPA = \frac{m_p c_p + m_s c_s}{m_p} \cdot \frac{\Delta T}{\Delta t} \qquad (1)$$

where $m_p$ and $m_s$ are the masses and $c_p$ and $c_s$ are the specific heats of the NPs and solvent, respectively. The term $\Delta T/\Delta t$ represents the slope of the initial increase in temperature.

## 3. Results and Discussion

The morphology of CO-NPs clearly points out a strong tendency of the NPs to create aggregates on a scale of several hundreds of nanometers, as visible in the bright field TEM image taken at a low (25 k) magnification (Fig 2a). As can be observed from HREM image (Fig. 2b), the obtained sample consists of nanoparticles of nearly spherical shape with homogeneous size distribution centered around 7 nm. Each particle is a single crystal of magnetite, as clearly pointed out by the FFT of the particle in the center of the HREM image (inset).

The TEM analysis performed on TD-NPs points out that the obtained samples consist of well-stabilized nanoparticles of spherical shape (Fig. 2d). Each particle is a single crystal of magnetite, as clearly indicated by atomic lattice fringes in HREM image and the spots in the FFT of the particle in the center of the image (Fig. 2e). The particles have a homogeneous and narrow size distribution centered around 6.5 nm (Fig. 2f). ED from a large area of the sample was employed to achieve structural information about the nanoparticles. In particular, the positions of the peaks and their relative intensities very well match the typical ones of magnetite powder (ICSD#: 082451), for both the investigated sample. In Fig. 3a the ED pattern obtained for the co-precipitated sample is reported; the relative intensities spectra obtained integrating the diffraction rings is given in Fig. 3b.

The hysteresis loops measured with an applied static field, reported in Fig. 4a, show for both samples zero coercivity and remanence, highlighting a superparamagnetic behavior at RT. CO-NPs show a very high saturation magnetization $(M_s)$ of 77 Am$^2$/kg, which is very close to the bulk value, while TD-NPs have a $M_s$ of 60 Am$^2$/kg. $M_s$ values were evaluated after the subtraction of the organic shell weight, previously estimated by Thermo Gravimetric Analysis (TGA). The relatively small difference in $M_s$ can be attributed to a higher crystallinity degree of the magnetic CO-NPs.[41]

In order to have a deeper insight into magnetic properties at RT, ZFC-FC measurements have been performed with an applied field of 7.96 kA/m. Fig. 4b shows two very different moment Vs. temperature dependences.
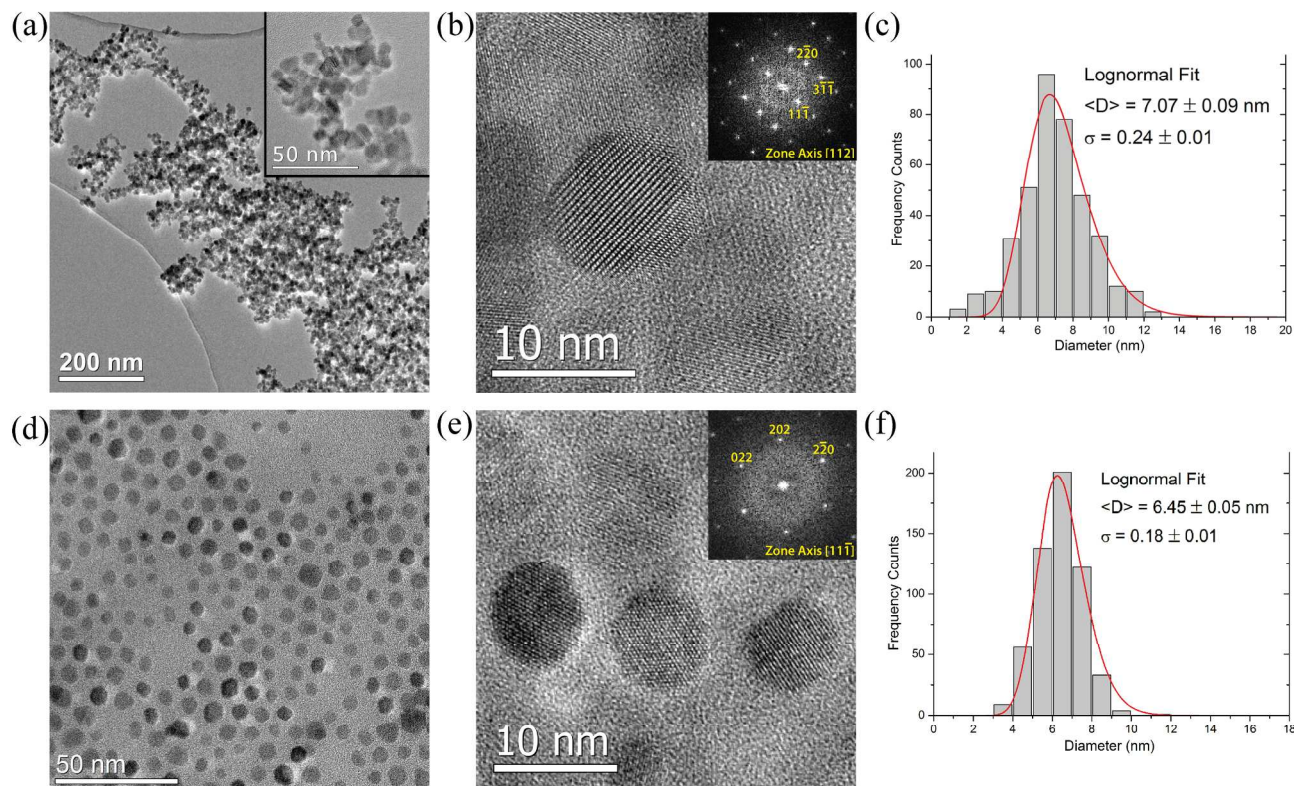
# Journal Name

## RSCPublishing

## ARTICLE

**Fig. 2** TEM characterization of magnetite NPs. (a) Low magnification bright field image (in the inset a highly magnified area is shown), (b) HREM image and (c) size distribution of NPs synthetized by co-precipitation. (d) Low magnification bright field image, (e) HREM image and (f) size distribution of NPs synthetized by thermal decomposition. The insets in (b) and (e) show the FFT of a square area containing the NP in the center of the image.
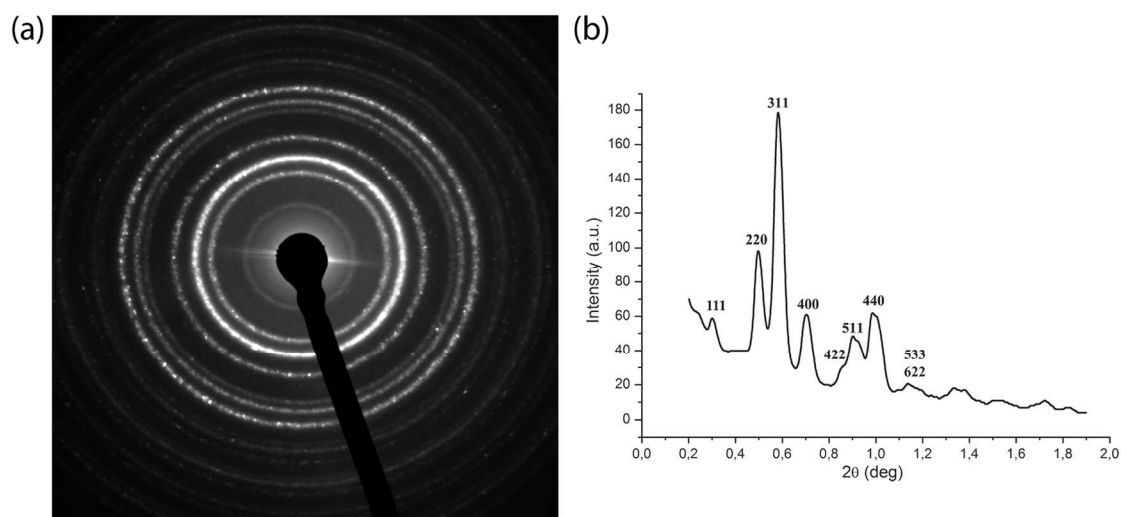


**Fig. 3** (a) Electron diffraction pattern obtained for the co-precipitated NPs. (b) Intensities spectrum obtained by integrating the diffraction rings; the main reflections are indexed.

# Journal Name

## ARTICLE

Nanoparticle size distributions of the two samples are very similar; however, TD-NPs are less interacting than CO-NPs, due to the organic shell. No steric stabilization is in fact present in the co-precipitated nanoparticles. In this case, as can be observed in Fig. 2a, the magnetic NPs are in contact. From DLS measurements a broad distribution of hydrodynamic diameters has been observed, peaked around 194 nm ($\sigma$ = 0.49); on the contrary, the particles obtained by thermal decomposition show a narrow distribution centered around 20 nm ($\sigma$ = 0.24).

In agreement with the observed values of hydrodynamic diameters, ZFC-FC measurements indicate very different magnetic behaviors in the two cases (Fig. 4b). CO-NPs sample shows a broad distribution of blocking temperatures and a flat FC curve, while the TD-NPs sample shows more typical lambda-shaped curves. In the latter case, the characteristic temperatures (as defined in Section 2.2) can be easily evaluated: $T_S$ = 25 ± 3 K, $T_B$ = 38 ± 2 K, $T_I$ = 51 ± 2 K. The very narrow size distribution of the NPs and the shape of ZFC-FC measurement highlight that the dipolar interactions in this system are less effective thanks to the organic shell (Fig. SI.2), which allows the nanoparticles to be well separated with mean inter-particle distances of 2-3 nm (Fig. 2d).

On the contrary, CO-NPs show higher $T_B$ and a flat FC curve in the whole temperature range, a typical curve for a system with strong dipolar interactions that produce an increase of the relaxation times.[42] The larger $T_B$ of CO-NPs compared to TD-NPs cannot simply reflect a larger magnetic anisotropy in the former sample, since the hysteresis loops measured in the blocked state (Figure 1 of the supplementary information file) do not evidence a substantial difference in anisotropy between the two samples, giving coercive field values of 26 mT for CO-NPs and 33 mT for TD-NPs.

The coherence between TEM and DLS results demonstrates that, in our specific case, the aggregation state of the NPs in the fluid suspension and after being deposited on a TEM grid is similar.

The subsequent step of our study was the hypertermic characterization of the samples. Hyperthermia measurements have been realized on both samples with a maximum applied field of 12.7 kA/m at 235 kHz (Fig. 4c). The calculated SPA values are 3.4 W/g and 50 W/g for TD-NPs and CO-NPs, respectively. Taking into account that published data refer to systems with variable interaction degrees and to different measurements parameters (i.e., field, frequency),[12-15, 43-47] our SPA values are compatible with those reported in the literature for NPs of the same size. However, the huge difference between the hypertermic response of TD-NPs and CO-NPs is quite surprising considering that the particle size distributions and $M_s$ values for the two systems are comparable. The only

possible explanation is that this difference originates from the establishing of strong dipolar interactions among the CO-NPs, as suggested by the ZFC-FC measurements (Fig. 4b).
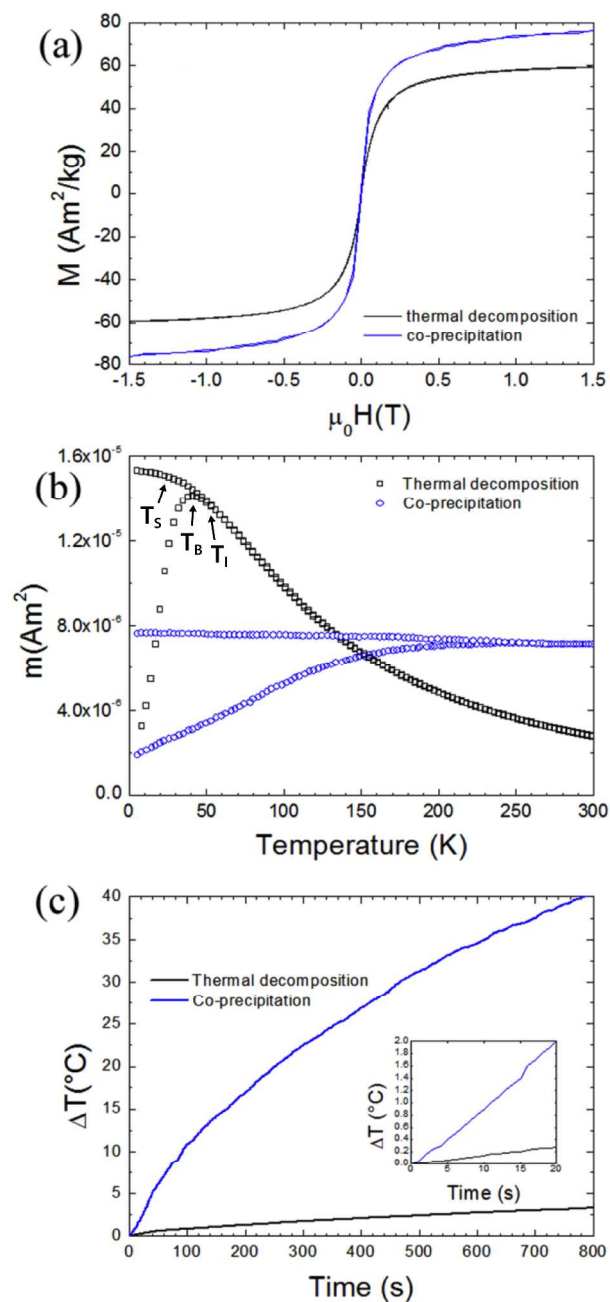


**Fig. 4** (a) Magnetization loops at room temperature (b) ZFC-FC and (c) variation of temperature as a function of time for magnetic NPs obtained by thermal decomposition and co-precipitation. The inset in (c) shows the initial slope of the curves.

In order to interpret such a difference, we have evaluated the energy barrier from ZFC-FC curves. The maximum energy barrier is given by

$$\Delta = k_B T_I \times \ln(\tau_m/\tau_0) \qquad (2)$$

where $k_B$ is the Boltzmann constant, $T_I$ is the maximum blocking temperature, $\tau_m$ is the measurement time and $\tau_0$ the attempt time. Considering $\tau_m$ of a magnetometer (100 s) and the classical value of $\tau_0 = 10^{-9}$ s, the above expression gives

$$\Delta = 25\, k_B T_I \qquad (3)$$

which corresponds to $1.7 \times 10^{-20}$ J for TD-NPs ($T_I=51$ K) and $7 \times 10^{-20}$ J for CO-NPs ($T_I$ is the blocking temperature of the largest aggregates, $\approx 200$ K). $\Delta$ is therefore enhanced in the CO-NPs sample and we will show below how this enhancement can affect the SPA.

The above $\Delta$ values can be used to estimate the blocking temperatures of the two particles ensembles in the hyperthermia experiments, which were performed at 235 kHz, i.e., with a measurement time $\tau_m$ of $6.77 \times 10^{-7}$ s. Inserting $\Delta$ and $\tau_m$ values in equation (2), blocking temperature values of 189 K and 780 K can be obtained for TD-NPs and CO-NPs, respectively.

This result supports the substantially different behavior of the two samples at RT. In the first case (TD-NPs) the sample is expected to be in the superparamagnetic regime also at high frequency (i.e. 235 kHz). Néel and Brown mechanisms are responsible for heat generation during magnetic hyperthermia experiments, giving rise to moderate SPA values. In the second case, due to the frequency-induced increase of blocking temperature, the big aggregates are in the blocked regime. The contribution to heat generation is given by magnetic hysteresis losses (area of the hysteresis loop), giving rise to much higher SPA values.
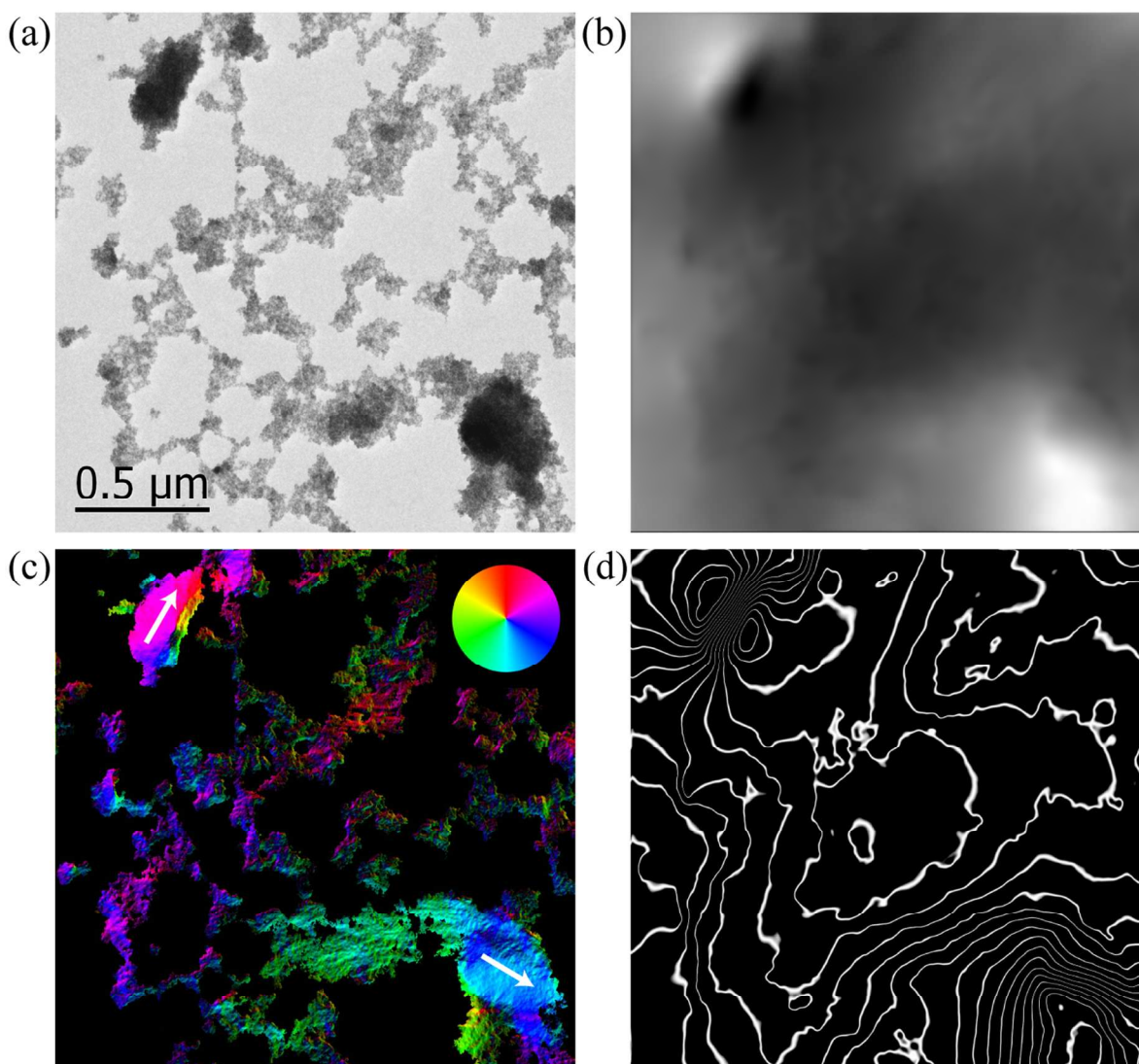


**Fig. 5** (a) Low magnification bright field image of co-precipitated NPs, showing the presence of big aggregates and linear aggregates. (b) Magnetic phase shift. (c) In-plane projected magnetic induction map and (d) distribution of magnetic flux, approximated by contour maps 10x amplified, obtained by Lorentz microscopy.
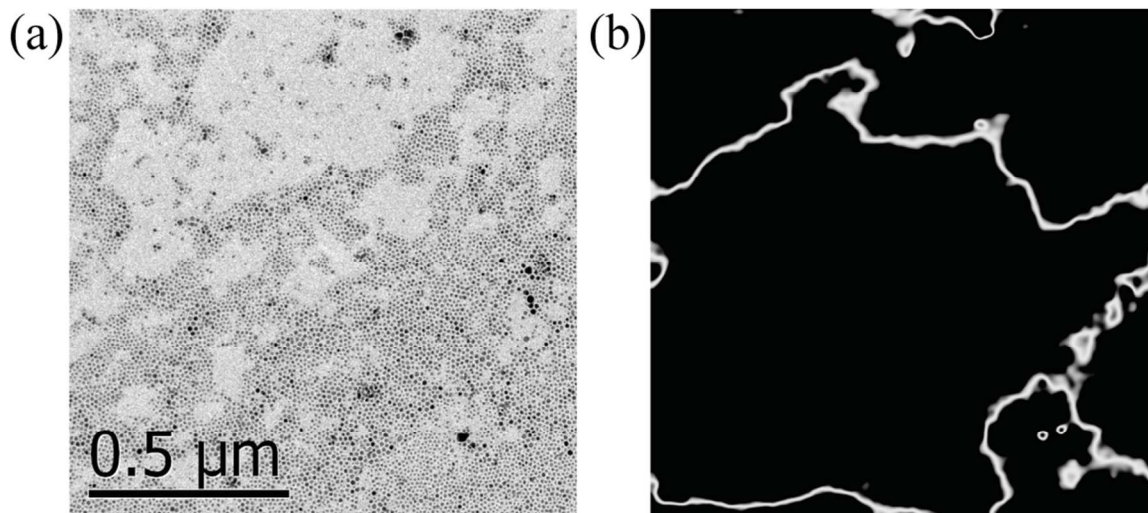
# Journal Name

## ARTICLE



**Fig. 6** (a) Low magnification bright field image of highly stabilized NPs, synthetized by thermal decomposition and (b) magnetic induction flux lines, approximated by contour maps 10x amplified, obtained by Lorentz microscopy.

In order to visualize and map the interactions at the basis of this huge difference in the SPA values we exploited Lorentz microscopy, a very powerful tool that allows retrieving the phase of the electron wave function and reconstructing the in-plane magnetic induction among different magnetic NPs and aggregates. Lorentz microscopy performed on CO-NPs evidences the presence of big magnetized aggregates, in which the magnetic moment of each nanoparticle has a preferential orientation along a common direction. The in-focus image of a significant area of the sample is reported in Fig 5a; the field of view of the image is 1.93 x 1.93 $\mu m^2$ and the image is representative of the whole sample. The magnetic phase shift relative to the same area of the sample is reported in Fig. 5b, while the mean inner potential is reported in Figure 3 of the supplementary information file. The magnetic induction color map (Fig. 5c), in which the regions not containing nanoparticles have been masked to simplify the visualization of the magnetic properties of different aggregates, clearly indicates that the big aggregates show a uniform magnetization in the directions depicted by the white arrows. Among the big aggregates, irregular NPs linear aggregates arise probably induced by drying the suspension in the dipolar field of the bigger aggregates; these irregular linear aggregates in fact do not show a uniform magnetization in the magnetic induction color map. From the cosine map of the 10x-amplified magnetic phase shift (Fig. 5d), which shows the flux-lines of the in-plane projected magnetic induction, it is possible to observe that the big aggregates generate a dipolar-like field, while the smaller magnetic linear aggregates do not perturb significantly the magnetic field lines of the bigger aggregates. On the contrary,

the flux lines generated by the big aggregates show a remarkable tendency to concentrate on the magnetic material among them.

It is possible to conclude that, even if the sample shows a macroscopic superparamagnetic behavior, in the bigger aggregates (which appear as magnetic dipoles) the magnetic interactions induce the moment of each nanoparticle to have a preferential orientation, correlated to the orientation of the other moments inside the aggregates. The superparamagnetic behavior of nanoparticles inside big aggregates is therefore highly affected by strong dipolar interactions and this effect has to be taken into consideration to correctly describe the hyperthermic behavior of the sample. This is also confirmed by the very large value of $\Delta$ evaluated assuming $T_I \sim 200$ K.

The Lorentz microscopy analysis performed on a significant area of the TD-NPs sample clearly points out that the highly stabilized NPs are in the superparamagnetic regime (the in-focus image of the focal series is reported in Fig. 6a; the field of view of the image is 1.27 x 1.27 $\mu m^2$). In this case the weak dipolar interactions among the NPs does not affect the magnetic behavior of the system, since no significant features in the cosine map of the 10x amplified magnetic phase shift can be related to the NPs (Fig. 6b).

From the above results, it is possible to assert that for the TD-NPs, the organic shell hinders the establishing of strong inter-particle interactions, in this way allowing the magnetic moments to be free to rotate inside the crystals. The SPA value is therefore mainly due to the Néel relaxation mechanism. Different is the behavior of the NPs obtained through co-precipitation, which are characterized by strong inter-particle

interactions giving rise to big aggregates interconnected by linear aggregates. The results obtained by using Lorentz microscopy demonstrate that:

- Big aggregates show a dipole-like behavior. Under a static magnetic field they do not show any hysteresis. Under an applied AC field at 235 kHz they are in the blocked regime and, consequently, give much higher SPA values due to hysteresis losses. This high-frequency induced blocking is coherent with what reported in Ref. 26.

- Nanoparticles external to the big aggregates do not show peculiar features attributable to a dipolar-like behavior. They show superparamagnetic properties and, thanks to the dipolar field generated by the big aggregates, they organize in linear aggregates. Their moments are free to rotate under an applied magnetic field, giving rise to a contribution to the SPA mainly due to Néel and Brown relaxation losses.

## 4. Conclusions

In this work spherical magnetite NPs with diameter of 6.5 - 7 nm have been synthetized by two different chemical routes, co-precipitation and thermal decomposition, in order to vary the degree of inter-particle interactions.

A careful analysis by means of TEM and Lorentz microscopy has evidenced that: (i) the particles obtained by both chemical routes are single-crystals of magnetite, (ii) those obtained by co-precipitation tend to form big aggregates with the establishing of strong inter-particle dipolar interactions, (iii) the particles obtained by thermal decomposition are well distributed and separated thanks to the inter-particle spacing provided by the organic surfactant, which reduces the dipolar interactions between the nanoparticles.

The hypertermic response of the NPs sample has been evaluated. Although both the described systems show superparamagnetic properties at room temperature and a comparable saturation magnetization under an applied static field, the SPA value for the co-precipitated NPs is an order of magnitude larger than the one of the NPs obtained by thermal decomposition. This remarkable difference in the SPA values can be explained considering that the NPs obtained by co-precipitation are strongly interacting and form big aggregates of hundreds nanometers, which are interconnected by linear aggregates of superparamagnetic nanoparticles. NPs synthetized by thermal decomposition are instead weakly interacting and well separated. The different morphology of the aggregates also reflects on their magnetic behavior, as revealed by Lorentz microscopy. The big aggregates in fact show a dipolar-like behavior, thus demonstrating that strong dipolar interactions in highly agglomerated NPs can affect the superparamagnetic regime with the establishing of a preferential orientation of the NPs moments. On the contrary, no preferential orientation of the moments of the NPs inside the linear aggregates is observed.

On the basis of the presented results, we can conclude that the SPA for the co-precipitated nanoparticles is due to two different contributions: a dominant hysteresis-loss dominated contribution, due to the big aggregates, and a smaller contribution originating from Néel and Brown relaxation losses, which arise as a consequence of the formation of nanoparticle linear aggregates.

## Acknowledgements

## Notes and references

[a] Istituto Materiali per l'Elettronica ed il Magnetismo IMEM-CNR, Parco Area delle Scienze 37/A, 43124 Parma, Italy. Fax: +39 0521269206; Tel: +39 0521269250; e-mail: marco.campanini@imem.cnr.it.

[b] Dipartimento di Chimica, Università di Parma, Parco Area delle Scienze 17/A, 43124 Parma, Italy.

[c] Instituto de Nanociencia de Aragón, Campus Río Ebro, Calle Mariano Esquillor, 50018 Zaragoza, Spain

1   A. Hervault and N. T. K. Thanh, *Nanoscale,* 2014, **6**, 11553.

2   H. B. Na, I. C. Song and T. Hyeon, *Adv. Mater.,* 2009, **21**, 2133.

3   F. Hu, K. W. MacRenaris, E. A. Waters, T. Liang, E. A. Schultz-Sikma, A. L. Eckermann and T. J. Meade, *J. Phys. Chem. C,* 2009, **113**, 20855.

4   O. T. Bruns, H. Ittrich, K. Peldschus, M. G. Kaul, U. I. Tromsdorf, J. Lauterwasser, M. S. Nikolic, B. Mollwitz, M. Merkel and N. C. Bigall, *Nat. Nanotechnol.,* 2009, **4**, 193.

5   N. Lee, Y. Choi, Y. Lee, M. Park, W. K. Moon, S. H. Choi and T. Hyeon, *Nano Lett.,* 2012, **12**, 3127.

6   Q. A. Pankhurst, N. K. T. Thanh, S. K. Jones and J. Dobson, *J. Phys. D: Appl. Phys.,* 2009, **42**, 224001.

7   M. Arruebo, R. Fernández-Pacheco, M. R. Ibarra and J. Santamaría, *Nanotoday*, 2007, **2**, 22.

8   M. Liong, J. Lu, M. Kovochich, T. Xia, S. G. Ruehm, A. E. Nel, F. Tamanoi and J. I. Zink, *ACS Nano*, 2008, **2**, 889.

9   T. Todd, Z. Zhen, W. Tang, H. Chen, G. Wang, Y. J. Chuang, K. Deaton, Z. Pan, and J. Xie, *Nanoscale*, 2014, **6**, 2073.

10  R. Hergt, S. Dutz, R. Müller and M. Zeisberger, *J. Phys.: Condens. Matter.*, 2006, **18**, S2919.

11  L. Asín, M. R. Ibarra, A. Tres and G. F. Goya, *Pharmaceut. Res.*, 2012, **29**, 1319.

12  E. Lima Jr, E. De Biasi, M. Vasquez Mansilla, M. E. Saleta, M. Granada, H. E. Troiani, F. B. Effenberger, L. M. Rossi, H. R. Rechenberg and R. D. Zysler, *J. Phys. D.: Appl. Phys.*, 2013, **46**, 045002.

13  M. Min Y. Wu, J. Zhou, Y. Sun, Y. Zhang, and G. Ning, *J. Magn. Magn. Mater.*, 2004, 268, 33.

14  G. F. Goya, T. S. Berquó, F.C. Fonseca and M. P. Morales, *J. Appl. Phys.*, 2003, **94**, 3520.

15  G. F. Goya, E. Lima, A. D. Arelaro, T. Torres, H. R. Rechenberg, L. Rossi, C. Marquina and M. R. Ibarra, *IEEE Trans. Magn.*, 2008, **44**, 4444.

Nanoscale Accepted Manuscript

16  P. Guardia, A. Riedinger, S. Nitti, G. Pugliese, S. Marras, A. Genovese, M. E. Materia, C. Lefevre, L. Manna and T. Pellegrino, *J. Mater. Chem. B*, 2014, **2**, 4426.

17  P. Guardia, R. Di Corato, L. Lartigue, C. Wilhelm, A. Espinosa, M. Garcia-Hernandez, F. Gazeau, L. Manna and T. Pellegrino, *ACS Nano*, 2012, **6**, 3080.

18  R. E. Rosensweig, *J. Magn. Magn. Mater.*, 2002, **252**, 370.

19  Y. Piñeiro-Redondo, M. Bañobre-López, I. Pardiñas-Blanco, G. F. Goya, M. A. López-Quintela and J. Rivas, *Nanoscale Res. Lett.*, 2011, **6**, 383.

20  A. Figuerola, R. Di Corato, L. Manna and T. Pellegrino, *Pharmacol. Res.*, 2010, **62**, 126.

21  A. Urtizberea, E. Natividad, A. Arizaga, M. Castro and A. Mediano, *J. Phys. Chem. C*, 2010, **114**, 4916.

22  P. de la Presa, Y. Luengo, M. Multigner, R. Costo, M. P. Morales, G. Rivero and A. Hernando, *J. Phys. Chem. C*, 2012, **116**, 25602.

23  D. Serantes, D. Baldomir, C. Martinez-Boubeta, K. Simeonidis, M. Angelakeris, E. Natividad, M. Castro, A. Mediano, D.-X. Chen, A. Sanchez, LI. Balcells and B. Martínez, *J. Appl. Phys.*, 2010, **108**, 073918.

24  M. E. Sadat, R. Patel, S. L. Bud′ko, R. C. Ewing, J. Zhang, H. Xu, D. B. Mast and D. Shi, *Mater. Lett.*, 2014, **129**, 57.

25  C. Martinez-Boubeta, K. Simeonidis, D. Serantes, I. Conde-Leborán, I. Kazakis, G. Stefanou, L. Peña, R. Galceran, L. Balcells, C. Monty, D. Baldomir, M. Mitrakas and M. Angelakeris, *Adv. Funct. Mater.*, 2012, **22**, 3737.

26  F. Burrows, C. Parker, R. F. L. Evans, Y. Hancock, O. Hovorka and R. W. Chantrell, *J. Phys. D: Appl. Phys.*, 2010, **43**, 474010.

27  M. Jeun, S. Bae, A. Tomitaka, Y. Takemura, K. H. Park, S. H. Paek and K.-W. Chung, *Appl. Phys. Lett.*, 2009, 95, 082501.

28  G. T. Landi, *Phys. Rev. B*, 2014, **89**, 014403.

29  K. Yamamoto, S. A. Majetich, M. R. McCartney, M. Sachan, S. Yamamuro and T. Hirayama, *Appl. Phys. Lett.*, 2008, **93**, 082502.

30  M. Varón, M. Beleggia, T. Kasama, R. J. Harrison, R. E. Dunin-Borkowski, V. F. Puntes and C. Frandsen, □*Sci. Rep.*, 2013, **3**, 1234.

31  Y. Takeno, Y. Murakami, T. Sato, T. Tanigaki, H. S. Park, D. Shindo, R. M. Ferguson and K. M. Krishnan, *Appl. Phys. Lett.*, 2014, **105**, 183102

32  R. Massart, *IEEE Trans. Magn.*, 1981, **17**, 1247.

33  S. Sun, H. Zeng, D. B. Robinson, S. Raoux, P. M. Rice, S. X. Wang and L. Guanxiong, *J. Am. Chem. Soc.,* 2004, **126**, 273.

34  K.O'Grady and A. Bradbury, *J. Magn. Magn. Mat.*, 1983, **39**, 91.

35  C. G. Granqvist and R. A. Buhrman, *J. Appl. Phys.,* 1976, **47**, 2200.

36  V. V. Volkov and Y. Zhu, *Phys. Rev. Lett.*, 2003, **91**, 043904.

37  V. Grillo, F. Rossi, *Ultramicroscopy*, 2013, **125**, 112.

38  V. Grillo, E. Rotunno, M. Campanini, M. C. Spadaro and S. D'Addato, *Microscopy and Microanalysis*, 2014, **20**, 2134.

39  E. Humphrey, C. Phatak, A.K. Petford-Long, M. De Graef, *Ultramicroscopy*, 2014, **139**, 5.

40  P.A. Hassan, S. Rana, G. Verma, *Langmuir,* 2015, **31**, 3.

41  C. Ravikumar and R. Bandyopadhyaya, *Journal Phys. Chem. C,* 2011, **115**, 1380.

42  M. Knobel, W. C. Nunes, L. M. Socolovsky, E. De Biasi, J. M. Vargas and J. C. Denardin, *J. Nanosci. Nanotechnol.*, 2008, **8**, 6, 2836.

43  G. Vallejo-Fernandez, O. Whear, A. G. Roca, S. Hussain, J. Timmis, V. Patel and K. O'Grady, *J. Phys. D: Appl. Phys.*, 2013, **46**, 312001.

44  M. E. Sadat, R. Patel, J. Sookoor, S. L. Bud'ko, R. C. Ewing, J. Zhang, H. Xu, Y. Wang, G. M. Pauletti, D. B. Mast, D. Shi, *Mater. Sci. Eng. C*, 2014, **42**, 52.

45  M. A. Gonzalez-Fernandez, T. E. Torres, M. Andrés-Vergés, R. Costo, P. de la Presa, C. J. Serna, M. P. Morales, C. Marquina, M. R. Ibarra, G. F. Goya, *J. Solid State Chem.*, 2009, **182**, 2779.

46  S. Larumbe, C. Gómez-Polo, J. I. Pérez-Landazábal and J. M. Pastor, *J. Phys. Condes. Matter.*, 2012, **24**, 266007.

47  R. Hergt, W. Andrä, C. G. d'Ambly, I. Hilger, W. A. Kaiser, U. Richter, H.-G. Schmidt, *IEEE Trans. Magn.*, 1998, **34**, 3745.

**Nanoscale Accepted Manuscript**